



CAD-Unet: A Capsule Network-Enhanced Unet Architecture for Accurate Segmentation of COVID-19 Lung Infections from CT Images

Yijie Dang^a, Weijun Ma^{a,b,*}, Xiaohu Luo^c

^aSchool of Information Engineering, Ningxia University, Yinchuan, 750021, Ningxia, China

^bNingxia Key Laboratory of Artificial Intelligence and Information Security for Channeling Computing Resources from the East to the West, Ningxia University, Yinchuan, 750021, Ningxia, China

^cSchool of Computer and Information Science, Southwest University, Chongqing, 400715, China

ARTICLE INFO

Article history:

Received 1 May 2013

Received in final form 10 May 2013

Accepted 13 May 2013

Available online 15 May 2013

Communicated by S. Sarkar

2000 MSC: 41A05, 41A10, 65D05, 65D17

Keywords: Medical image segmentation, COVID-19, Convolutional neural network, Capsule network

ABSTRACT

Since the outbreak of the COVID-19 pandemic in 2019, medical imaging has emerged as a primary modality for diagnosing COVID-19 pneumonia. In clinical settings, the segmentation of lung infections from computed tomography images enables rapid and accurate quantification and diagnosis of COVID-19. Segmentation of COVID-19 infections in the lungs poses a formidable challenge, primarily due to the indistinct boundaries and limited contrast presented by ground glass opacity manifestations. Moreover, the confounding similarity between infiltrates, lung tissues, and lung walls further complicates this segmentation task. To address these challenges, this paper introduces a novel deep network architecture, called CAD-Unet, for segmenting COVID-19 lung infections. In this architecture, capsule networks are incorporated into the existing Unet framework. Capsule networks represent a novel network architecture that differs from traditional convolutional neural networks. They utilize vectors for information transfer among capsules, facilitating the extraction of intricate lesion spatial information. Additionally, we design a capsule encoder path and establish a coupling path between the unet encoder and the capsule encoder. This design maximizes the complementary advantages of both network structures while achieving efficient information fusion. Finally, extensive experiments are conducted on four publicly available datasets, encompassing binary segmentation tasks and multi-class segmentation tasks. The experimental results demonstrate the superior segmentation performance of the proposed model. The code has been released at: <https://github.com/AmanoTooko-jie/CAD-Unet>.

© 2024 Elsevier B. V. All rights reserved.

1. Introduction

Since the outbreak of the novel coronavirus disease (COVID-19) in 2019, healthcare systems worldwide have faced tremendous pressure. In such a critical situation, timely and accurate diagnosis is crucial for effective patient management.

Currently, reverse transcriptase-polymerase chain reaction (RT-PCR) is considered as the gold standard of diagnosing COVID-19 for its high specificity (Wang et al., 2020b). While PCR testing serves as the primary clinical diagnostic test, it is not without certain limitations. Firstly, the implementation of PCR testing poses challenges in resource-limited settings or remote areas due to its requirement for specialized laboratory facilities and skilled personnel, which are often scarce in such environments. Secondly, the turnaround time for PCR results can

*Corresponding author.

e-mail: weijunma_2008@sina.com (Weijun Ma)

be relatively long, ranging from a few hours to days, which may hinder timely decision-making and patient management. Finally, a limitation is the potential for false negatives. Factors such as improper sample collection, variations in viral load during different stages of infection, or technical errors in the PCR process, which can contribute to false-negative results, leading missed diagnoses and potential virus transmission (Ai *et al.*, 2020). To address these challenges, medical imaging techniques have been extensively utilized as a primary or adjunctive tool (Vantaggiato *et al.*, 2021).

Among many medical imaging techniques, computed tomography (CT) imaging has emerged as a valuable tool in the detection and assessment of COVID-19 (Kucirka *et al.*, 2020), offering detailed insights into the extent and severity of lung involvement. CT scans of COVID-19 patients commonly exhibit distinctive radiological patterns, such as ground-glass opacities (GGOs), consolidations (CONs), and crazy-paving patterns, as well as various other features. GGO, characterized by an increased density in lung regions with a hazy shadow reminiscent of glass transparency, presents as high-opacity areas with blurred margins on CT scans. CON, characterized by increased density due to inflammatory exudates or hemorrhage filling alveoli, appears as denser, solid white areas, with potential for clear or blurred edges. Crazy-paving patterns, displaying thickened alveolar walls and increased interstitial texture due to edema and inflammation, exhibit an intricate, brick-like interlocking pattern on CT images. This variability poses difficulties for radiologists in accurately segmenting and distinguishing infected areas from normal lung tissue. As a result, the pursuit of automated segmentation techniques for COVID-19 lung CT images has garnered significant attention in recent years. Automated segmentation of lung regions from CT scans plays a crucial role in quantifying the extent of lung involvement, assisting in disease diagnosis, monitoring disease progression, and evaluating treatment response. It enables the extraction of quantitative features, such as lesion volume and density, which can aid in patient risk stratification and treatment planning (Lei *et al.*, 2020; Ng *et al.*, 2020; Pan *et al.*, 2020).

Over the years, various computerized methods have been proposed for lung segmentation in CT images, ranging from traditional image processing algorithms to advanced machine learning techniques. Deep learning, particularly convolutional neural networks (CNNs), has emerged as a dominant approach in medical image segmentation, demonstrating promising results in various applications.

However, the complex and variable nature of COVID-19 lesions within the lungs presents significant challenges for automatic segmentation using deep learning techniques. COVID-19, caused by the SARS-CoV-2 virus, manifests in the lungs through diverse and highly variable pathological findings. Firstly, the size of COVID-19-associated lesions can vary considerably, with some patients exhibiting small, focal areas of infection, while others display widespread, diffuse involvement of multiple lung lobes. This variability necessitates deep learning models to possess a high degree of flexibility and adaptability to accurately segment these patterns. Secondly, the shapes and patterns of the lesions also exhibit significant diversity.

Ground-glass opacities (GGO) typically manifest as round or oval-shaped opacities, whereas consolidation (CON) may appear as irregular or patchy areas. In some cases, lesions may present with a mixed appearance, combining GGO with areas of consolidation or fibrosis. This heterogeneity in lesion morphology poses considerable challenges for deep learning models to consistently and accurately segment the infected regions. Finally, the location of lesions within the lungs can vary significantly, with some patients having lesions primarily in peripheral regions and others in more central locations. This spatial variability requires deep learning models to have a comprehensive understanding of lung anatomy and the potential locations of COVID-19 lesions.

In order to tackle the aforementioned challenges, we introduce an innovative deep network architecture called CAD-Unet designed specifically for CT slices. In this architecture, we couple capsule networks into the encoder stage of the Unet architecture to enhance the segmentation performance of the proposed network. Capsule networks can better preserve the relative spatial positional information between features, thereby enhancing their recognition capabilities for the varying sizes, complex shapes, and differentiated lesion locations exhibited by COVID-19 pulmonary lesions. This capability aligns with the fundamental principle of capsule networks, where information is stored and transmitted at the neuron level as vectors rather than scalars (LaLonde *et al.*, 2021). These vectors encapsulate details about the spatial attitude of objects, including their locations, scale locations, and orientations between different parts (Tran *et al.*, 2022). Furthermore, the implementation of a dynamic routing algorithm in capsule networks facilitates the transfer of information between capsule layers, allowing the model to effectively capture the positional relationships between objects. We conduct comprehensive comparative experiments using four publicly accessible datasets, illustrating the superior performance of the proposed architectural framework in the context of pulmonary infection segmentation.

In summary, the main contributions of this paper are:

- We introduce a dedicated network architecture designed to address the segmentation task of COVID-19 pulmonary CT lesions, with a particular focus on handling complex lesion shapes that are difficult to identify. This architecture integrates both capsule networks and U-Net, enhancing the model's capability to capture and encode critical information in lung CT images.
- We innovatively design the integration of capsule networks pathway and U-Net encoder pathway in parallel, coupled through a pathway coupling mechanism. This design not only maximizes the complementary strengths of the two network structures but also allows for efficient information fusion. The model learns and expresses features more comprehensively, excelling particularly in scenarios involving complex lesion shapes and ambiguous boundaries.
- We conduct extensive experiments on four publicly available datasets, including both binary segmentation tasks and multi-class segmentation tasks, and compare the proposed architecture against three baseline architectures

(Unet (Ronneberger et al., 2015), UNet++ (Zhou et al., 2018), Att-Unet (Oktay et al., 2018)) and four state-of-the-art COVID-19 segmentation architectures (binary segmentation: InfNet (Fan et al., 2020), SCOAT-Net (Zhao et al., 2021), nCoVSegNet (Liu et al., 2021), and PDEAtt-Unet (Bougourzi et al., 2023b), multi-class segmentation: CopleNet (Wang et al., 2020a), AnamNet (Paluru et al., 2021), SCOAT-Net (Zhao et al., 2021), and D-TrAttUnet (Bougourzi et al., 2023a)). The experimental results demonstrate that the proposed architecture exhibits strong segmentation performance in both binary and multi-class segmentation, outperforming the strong baselines and state-of-the-art medical image segmentation methods.

2. Related works

The COVID-19 pandemic has sparked extensive research in the field of medical imaging, particularly in the domain of lung CT lesion segmentation. There are various methods for lung CT lesion segmentation. In this section, we will only discuss segmentation architectures based on Unet and the utilization of capsule networks for target segmentation.

2.1. Segmentation architecture based on Unet

The segmentation architecture based on Unet (Ronneberger et al., 2015) has found extensive application in the field of medical imaging, particularly for lung CT lesion segmentation tasks. Unet constitutes a classical CNNs architecture characterized by the concurrent presence of an encoder and a decoder. The encoder gradually extracts both low-level and high-level features from the image, while the decoder maps these features back to the image space, yielding intricate segmentation outcomes.

In the context of the COVID-19 pandemic, numerous researchers have adopted the Unet architecture for segmenting lesion regions in lung CT images, aiming to provide precise support for clinical diagnosis and disease monitoring. For instance, Chen et al. (2020) initially applied Unet++ (Zhou et al., 2018) to COVID-19 lung CT lesion segmentation. Unet++, an extension of the Unet framework, employs a series of nested and densely connected skip pathways between encoder and decoder subnetworks, further enhancing semantic relationships between them and achieving improved performance in lung CT lesion segmentation tasks. Zhao et al. (2021) reengineered the connection structure of Unet++ to propose SCOAT-Net, introducing a biologically motivated attention learning mechanism. This approach introduces specially designed spatial-wise and channel-wise attention modules, which collaborate to enhance the network's attention learning and consequently improve the segmentation accuracy. Building upon Unet, Bougourzi et al. (2023b) developed PDAAtt-Unet, a pyramid dual-decoder Att-Unet (Lian et al., 2018) architecture that utilizes pyramid structures and attention gates to maintain global spatial awareness across all encoding layers. During the decoding phase, PDAAtt-Unet incorporates two separate decoders employing attention gates to simultaneously segment infections and the lung region.

2.2. Capsule networks for object segmentation

Capsule networks, introduced by Sabour et al. (2017), have garnered significant attention within the field of object segmentation due to their unique architecture and potential to address certain limitations of traditional CNNs. In contrast to CNNs, that rely on pooling and hierarchical feature extraction, capsule networks aim to model the hierarchical relationships between features by representing them in the form of capsules.

The fundamental innovation of capsule networks lies in their ability to preserve spatial hierarchies and capture viewpoint information of objects. Traditional CNNs often struggle with handling variations in object poses and tend to rely heavily on the spatial pooling of features. Conversely, capsules within a capsule network encode multiple attributes of an object, such as pose, deformation, and texture, while also considering the relationships between these attributes. This makes capsule networks inherently suited for object segmentation tasks, where understanding spatial hierarchies and viewpoints is critical.

However, the original architecture of capsule networks and dynamic routing algorithm incurs significant computational expenses in terms of memory and runtime (LaLonde et al., 2021). In order to address this concern, LaLonde et al. (2021) extended the concept of convolutional capsules and redefined the dynamic routing algorithm in two crucial ways. Firstly, children capsules are selectively routed to parents capsules within a localized spatial kernel. Secondly, transformation matrices are shared among all members of the grid within a specific capsule type, yet not shared across different capsule types. Subsequently, a multitude of researchers have delved deeper into the exploration of capsule network models for the purpose of object segmentation. For instance, Survarachakan et al. (2020) developed the Multi-SegCaps model, EM-routing SegCaps model, and U-Net model capable of segmenting an arbitrary number of classes. These models were applied to the segmentation of individual 2D slices, utilizing two neighboring slices on each side (five in total). Tran et al. (2022) proposed the 3DConvCaps model, which employs capsule networks for 3D image segmentation. 3DConvCaps constitutes a 3D encoder-decoder network with a convolutional capsule encoder, facilitating the learning of lower-level features using convolutional layers (short-range attention), while simultaneously modeling higher-level features (long-range dependencies) with capsule layers.

In this paper, the integration of the two techniques has been undertaken with the aim of COVID-19 lung CT lesion segmentation. However, distinct from these previous investigations, the CAD-Unet establishes a path coupling between Unet-encoder and convolutional capsules, thereby fusing the strengths of convolution and capsules to extract target features. Moreover, the incorporation of attention gates and a dual decoder has been implemented. These modules collectively interact to significantly bolster the overall performance of the CAD-Unet architecture. Subsequently, a comprehensive elucidation of the proposed network architecture is furnished.

3. The proposed approach

Within this section, an extensive elucidation of the CAD-Unet network architecture, fundamental constituents of the net-

work, and the employed loss functions will be provided.

3.1. Network architecture

The overall architecture of CAD-Unet is illustrated in Fig. 1. Based on the foundational Unet framework, the capsule encoder path of capsule networks and the encoder path of Unet operate in parallel. Each layer of Unet incorporates ResBlocks to consolidate features. The decoder phase consists of two pathways: one for predicting the infected region, which serves as the final prediction, and the other for predicting the lung region, aiming to focus the network attention on the lung area since the infected region is exclusively present within the lung region. In the following sections, we will provide a detailed description of the core modules and loss functions employed in this network.

3.2. Convolutional capsule layer

Capsule networks, originally proposed by Sabour *et al.* (2017), consist of multiple capsule layers and innovatively represent the information transfer between capsule layers as vectors rather than scalars. These vectors not only encode specific entity types but also describe how entities are instantiated, including their postures, textures, deformations, and the presence of these features themselves Choi *et al.* (2019). Among them, the norm of the vector indicates the probability of the entity's existence, while the orientation of the vector indicates the configuration of the entity. Information between capsule layers is transmitted through a dynamic routing algorithm, which iteratively updates the weights between capsules, enabling higher-level capsules to effectively route the outputs of lower-level capsules. As a result, more accurate and robust feature representations are obtained. This dynamic routing mechanism is a key characteristics of capsule networks, allowing the network to learn hierarchical representations and spatial relationships of objects.

Using capsule-based networks for object segmentation poses several issues. The inherent complexity of the original capsule network architecture and dynamic routing algorithm results in significant computational demands, affecting memory usage and runtime performance (LaLonde *et al.*, 2021). To address these issues, LaLonde *et al.* (2021) proposed SegCaps, where they introduced capsule sharing for each category, effectively reducing the computational overhead. Specifically, as illustrated in 2, the input feature map size of the capsule layer is $H \times W \times C \times A$, where $H \times W$ represents the feature map dimensions, C is the number of capsule types, and A is the size of each capsule. Firstly, the capsule u_i for class i is linearly mapped to a higher-level feature \hat{u}_i using the same transformation matrix W . Then, all \hat{u}_i are weighted and summed to obtain the input s of the higher-level capsule. Finally, the squash function is applied to s to ensure that the vector direction remains unchanged while compressing the vector length between 0 and 1, representing the probability of entity presence. The dynamic

routing process can be represented (1) as follows:

$$\begin{aligned} \hat{u}_i &= W_i u_i, \\ s &= \sum_i c_i \hat{u}_i, \\ v &= \text{squash}(s), \\ \text{squash}(s) &= \frac{\|s\|^2}{1 + \|s\|^2} \frac{s}{\|s\|}, \end{aligned} \quad (1)$$

where i is the capsule category, u represents the input to the higher-level capsule, W is the transformation matrix, \hat{u}_i corresponds to the input of the higher-level capsule, c_i represents the coupling coefficients determined through the iterative dynamic routing process, and v denotes the output of the capsule at this layer. $\|\cdot\|$ denotes L_2 norm.

Linear mapping is achieved by the convolutional layer, where W actually represents the parameters of the convolutional kernels. The convolutional layer employs a kernel size of 5×5 with a stride of 2, which enables the completion of one down-sampling operation on the original feature map.

The coupling coefficients c_i between capsule categories are determined by the dynamic routing algorithm. This algorithm is an iterative process that updates the values of c_i through multiple rounds of iterations. The number of iterations r is a hyper-parameter and is set to 3 in our architecture.

3.3. Two parallel encoder pathways

COVID-19 lung lesions exhibit diverse morphologies in CT images, including infiltrations, nodules, and patchy patterns, among others. Solely utilizing convolutional networks for learning target region features has limitations, while capsule networks utilize vectors to convey information, enabling a better capture of target morphology. Additionally, the dynamic routing algorithm connects different layers of capsules, allowing for a better capture of contextual relationships between objects. This advantage empowers capsule networks to handle issues such as object relationships and hierarchical structures in images. Therefore, we innovatively couple capsule networks with convolution in parallel, leveraging the strengths of capsule networks to compensate for the limitations of convolution.

Specifically, in the encoder stage of the network, we design two parallel paths: the capsule encoder path and the Unet encoder path, and the feature information from these two paths interacts with each other. The input image $x \in \mathbb{R}^{H \times W \times C}$ is fed into both paths, where H and W represent the height and width of the input image, respectively, and C denotes the number of channels in the input image. Now, we will provide a detailed explanation of each path.

- (a) **Capsules encoder pathway:** In the capsule encoding pathway, we initially generate primary capsules through a convolutional layer with a kernel size of 5×5 , resulting in capsules of a single category $C_0 \in \mathbb{R}^{H \times W \times 1 \times 16}$. The primary capsule C_0 is then propagated to the primary capsule layer, which is a conventional convolutional capsule layer. It undergoes one routing iteration and returns 16-dimensional capsules for two categories, denoted as $C_1 \in \mathbb{R}^{\frac{H}{2} \times \frac{W}{2} \times 2 \times 16}$. Following this, at each stage, the convolutional capsule

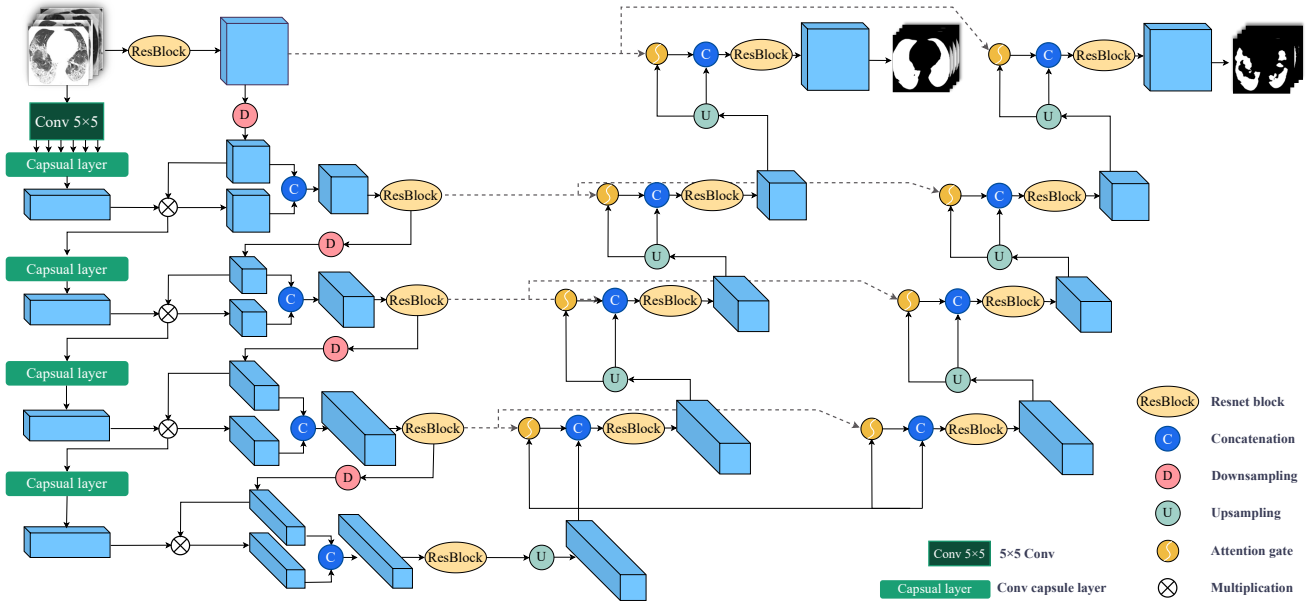


Fig. 1. Detailed structure of the proposed CAD-Unet architecture.

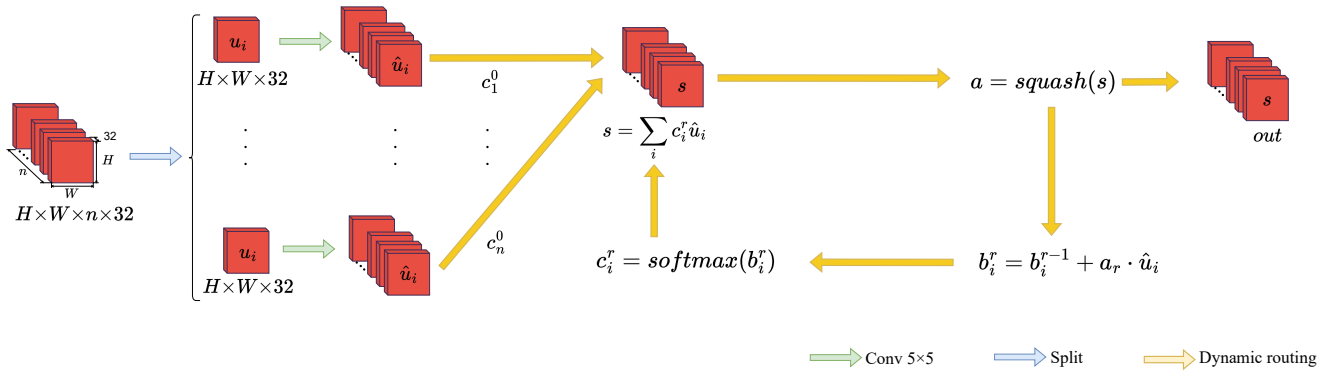


Fig. 2. Schematic description of convolutional capsule layer

layer is coupled with the results of different levels of the Unet pathway, gradually extracting higher-level semantic information, allowing the model to effectively comprehend the complex structure of input data. Specifically, C_1 is coupled with the first layer of the Unet pathway, the coupled result is then forwarded to the secondary capsule layer, comprising three routing iterations. The output consists of 32-dimensional capsules for two categories, denoted as $C_2 \in \mathbb{R}^{\frac{H}{4} \times \frac{W}{4} \times 2 \times 32}$, with capsule dimensions expanding similarly through convolutional capsule layer operations. Following this, C_2 is coupled with the results of the Unet pathway and transmitted to the tertiary capsule layer, returning 32-dimensional capsules for four categories, represented as $C_3 \in \mathbb{R}^{\frac{H}{8} \times \frac{W}{8} \times 4 \times 32}$. Finally, C_3 is coupled with the Unet pathway results and transmitted to the quaternary capsule layer, yielding 64-dimensional capsules for four categories, denoted as $C_4 \in \mathbb{R}^{\frac{H}{16} \times \frac{W}{16} \times 4 \times 64}$. It is observable that the size of the feature map is reduced by half and the number of channels is doubled after the convolutional capsule layer. The convolutional operations within the capsule

layer control the size of the output capsules, with a stride of 2 implemented for achieving a twofold downsampling. This approach enables the reduction of spatial dimensions and gradual increase in channel numbers in the feature map, facilitating the model in learning abstract hierarchical features. This process is expressed by equation (2):

$$\begin{aligned}
 C_0 &= Conv_{5 \times 5}(in), \\
 C_1 &= ConvCap(C_0), \\
 C_2 &= ConvCap(C_1 \cdot out_0), \\
 C_3 &= ConvCap(C_2 \cdot out_1), \\
 C_4 &= ConvCap(C_3 \cdot out_2),
 \end{aligned} \tag{2}$$

where $Conv_{5 \times 5}(\cdot)$ is the convolution operation with a 5×5 kernel, $ConvCap(\cdot)$ is the convolutional capsule layer, and in is the initial input to the network.

(b) **Unet encoder pathway:** In the Unet encoder pathway, we employ a Unet baseline architecture enhanced with

ResBlocks (Bougourzi *et al.*, 2023a). This architecture comprises layers, each consisting of a ResBlock and a downsampling module. The initial layer (Layer 0) receives the original network input, while subsequent layers receive the output of the previous layer and the pathway coupling results from the capsules pathway. Specifically, we perform point-wise multiplication between the predictions from each layer of the capsules pathway and the feature extraction from each layer of the Unet pathway. This strategic fusion enables the Unet pathway to seamlessly integrate features extracted from the capsules pathway, thereby enriching its contextual understanding. Let out_{l-1} represent the output of the previous layer, and the input to the current layer, denoted as in_l , is computed as $in_l = cat(out_{l-1}, out_{l-1} \cdot C_l)$. Here, in_l signifies the input to the l st layer, out_{l-1} is the output of the $(l-1)$ -th layer, C_l represents the output of the l st capsule layer, and cat denotes the concatenation operation along the channel dimension. Following this, this input undergoes a ResBlock to extract features, followed by passage through a max-pooling layer for downsampling, resulting in the output of this layer, as depicted in equation (3):

$$\begin{aligned}
in_0 &= ResBlock(in), out_0 = MP(in_0), \\
in_1 &= Cat(C_1 \cdot out_0, out_0), out_1 = MP(RB(in_1)), \\
in_2 &= Cat(C_2 \cdot out_1, out_1), out_2 = MP(RB(in_2)), \\
in_3 &= Cat(C_3 \cdot out_2, out_2), out_3 = MP(RB(in_3)), \\
in_4 &= Cat(C_4 \cdot out_3, out_3), out_4 = RB(in_4),
\end{aligned} \quad (3)$$

where in is the initial input to the network, in_l is the input of the l -th layer, out_l is the output of the l -th layer, C_l is the output of the l -th capsule layer, $Cat(\cdot)$ denotes the concatenation operation along the channel dimension, $MP(\cdot)$ represents passing through a max-pooling layer, and $RB(\cdot)$ represents passing through a ResBlock. As shown in Fig.3, the ResBlock consists of two 3×3 convolutional blocks, each followed by batch normalization and ReLU activation. Additionally, a residual connection is used to add the input to the output of the two convolutional layers. The residual connection consists of a 1×1 convolutional block, followed by batch normalization and ReLU activation as shown in equation (4):

$$\begin{aligned}
RB(x) &= Out_{Conv}(x) + Out_{Res}(x), \\
Out_{Conv}(x) &= ConvBlock(ConvBlock(x)), \\
Out_{Res}(x) &= ReLU(BN(Conv_{1 \times 1}(x))), \\
ConvBlock(x) &= ReLU(BN(Conv_{3 \times 3}(x))),
\end{aligned} \quad (4)$$

where x is the input to the ResBlock, $Conv_{n \times n}(\cdot)$ is the convolution operation with an $n \times n$ kernel, $BN(\cdot)$ is the batch normalization, and $ReLU(\cdot)$ is the ReLU activation function.

3.4. Attention gate

The conventional Unet framework incorporates skip connections that directly link low-level features from the encoder to

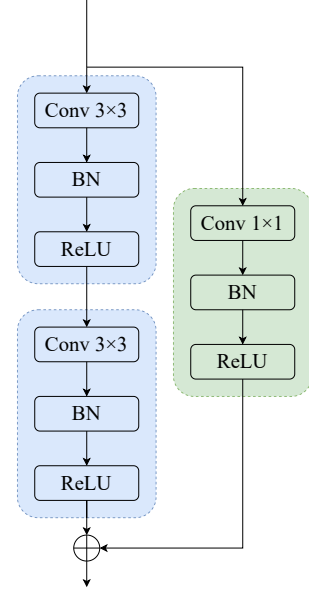


Fig. 3. The structure of ResBlock

high-level features in the decoder. However, this strategy introduces redundant and irrelevant information to the high-level features, adversely impacting the precision of target segmentation. Motivated by the Attention U-Net (Oktay *et al.*, 2018), we integrate attention gates into the proposed architecture to address this limitation. The attention gates selectively emphasize relevant features while suppressing redundant and less informative ones, which greatly improves segmentation accuracy. By adaptively weighting the contributions of encoder and decoder features, the attention mechanism enhances the model's capability to focus on crucial regions, thereby refining the segmentation outcomes.

The structure of the attention gate is elucidated in Fig.4. This module takes an input feature map $x \in R^{H \times W \times C_x}$ and a gate signal $g \in R^{H \times W \times C_g}$, where x signifies the output feature map of the encoder l -th layer, and g represents the output feature map of the decoder $(l + 1)$ -th layer. Subsequently, the feature map x and the gate signal g undergo linear transformations through 1×1 convolutional layers, followed by batch normalization and element-wise summation. Following this, the ReLU activation function is applied, and another 1×1 convolutional layer is utilized to derive spatial attention coefficients, denoted as Att for each pixel. Finally, these obtained attention coefficients are applied to the input feature map x , as expressed in equation (5):

$$\begin{aligned}
Att &= \psi_i(ReLU(BN(W_x x_i) + BN(W_g g_i))) \oplus F, \\
out_{AG} &= x_i \cdot Att,
\end{aligned} \quad (5)$$

where W_x and W_g are 1×1 convolutional operations used for linear transformations, and ψ_i is a 1×1 convolutional operation employed to generate spatial attention coefficients. out_{AG} represents the output of the attention gate module.

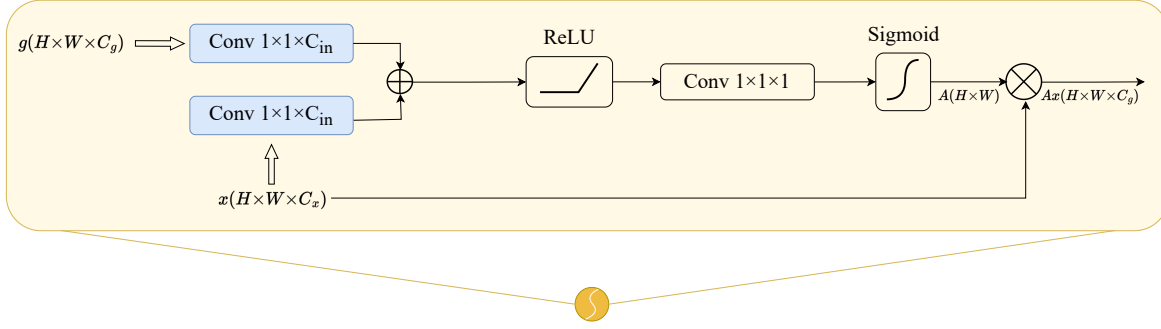


Fig. 4. Attention gate block, where g is the gating signal and the x is the input feature maps. A is the obtained spatial attention, which is applied for all channels of the input feature maps x .

3.5. Dual decoder

To focus the network on the infected regions, we employ the dual decoder used in DAtt-Unet (Bougourzi et al., 2023b). The dual decoder is designed to achieve simultaneous segmentation of both infections regions and lung regions. The objective is to guide the training process to explore the interior of the lung regions and differentiate between infected tissue and non-pulmonary tissue.

As shown in Fig.1, the decoder consists of two pathways: pathway 1 predicts the lung region, and pathway 2 predicts the infection region. The prediction results from pathway B serve as the final prediction target, while the existence of pathway A aims to guide the model focus on the lung region, as infection areas only occur within the lungs.

Specifically, except for the last layer, each layer in the decoder receives two inputs: the output from the previous layer of the decoder and the concatenated result of the attention gate output at the same layer. Similar to the encoder, these inputs undergo a ResBlock and an upsampling operation to become the current layer output. This output serves two purposes: 1) it is forwarded to the attention gate unit as the gating signal g , and 2) it is passed to the next layer of the decoder. The dual decoder process can be represented as equation (6):

$$d_{i,j} = RB_j(\text{Cat}_j(\text{AG}_j(\text{US}_j(d_{i-1,j}), x_{i,j}), \text{US}_j(d_{i-1,j}))), \quad (6)$$

$$i \in \{0, 1, 2, 3, 4\}, j \in \{1, 2\},$$

where i represents the layer index, and j represents the decoder pathway number. d_i denotes the output of the i -th layer of the decoder, and x_i represents the output of the i -th layer of the encoder. The upsampling operation is denoted by US, and AG represents the attention gate unit. It is essential to note that the two pathways of the decoder do not share any modules, including the attention gate unit.

3.6. Hybrid loss function

For CT lung lesion segmentation tasks, the complex morphology of the target region edges poses issue for accurate segmentation. Existing research has shown that edge information can provide valuable constraints to guide feature extraction for segmentation (Zhao et al., 2019; Wu et al., 2019; Zhang et al., 2019). Therefore, we employ the hybrid loss function proposed

in PDEAttUnet (Bougourzi et al., 2023b) to guide the network training, which consists of three components: 1) infection segmentation loss (\mathcal{L}_{Inf}) for the final task prediction, 2) lung segmentation loss (\mathcal{L}_{Lung}) to assist in the final prediction of lung regions, and 3) edge loss (\mathcal{L}_{Edge}) to enhance the segmentation of target edges. The hybrid loss function is formulated as equation (7):

$$\mathcal{L}_{All} = \alpha \mathcal{L}_{Inf} + \beta \mathcal{L}_{Lung} + \gamma \mathcal{L}_{Edge},$$

$$\mathcal{L}_{Inf} = - \sum_{m=1}^B \sum_{i=1}^{W \cdot H} G_{R_i} \log(p_i) + (1 - G_{R_i}) \log(1 - p_i),$$

$$\mathcal{L}_{Lung} = - \sum_{m=1}^B \sum_{i=1}^{W \cdot H} G_{L_i} \log(s_i) + (1 - G_{L_i}) \log(1 - s_i), \quad (7)$$

$$\mathcal{L}_{Edge} = - \sum_{m=1}^B \sum_{i=1}^{W \cdot H} G_{E_i} \log(P_{E_i}) + (1 - G_{E_i}) \log(1 - P_{E_i}),$$

where α , β , and γ are the weights for the infection segmentation loss (\mathcal{L}_{Inf}), lung segmentation loss (\mathcal{L}_{Lung}), and edge loss (\mathcal{L}_{Edge}), respectively. W and H represent the width and height of the predicted mask, and B is the batch size. The ground truth labels for infection and lung of pixel i are denoted as $G_{R_i} \in \{0, 1\}$ and $G_{L_i} \in \{0, 1\}$, respectively. Additionally, p_i and s_i represent the prediction probabilities of infection and lung for pixel i , obtained from the decoders used for segmenting infection and lung, respectively. On the other hand, foredge loss function, $G_{E_i} \in \{0, 1\}$ and P_{E_i} are the ground truth label and the predicted probability of edge infection for pixel i , respectively. The ground-truth edge pixels are derived by applying morphological gradient to the ground-truth infection regions. Once the ground-truth edge pixels are obtained, the binary cross entropy (BCE) loss function is employed to compute the loss between the ground-truth edge pixels and their corresponding pixels in the mask map. The weight γ of the edge loss is determined through experimental evaluation for each dataset.

4. Experiments and results

4.1. Dataset

The proposed method is evaluated on four publicly available datasets, namely COVID-19 CT segmentation (Radiologists,

2019), segmentation dataset nr.2 (Radiologists, 2019), COVID-19-CT-Seg dataset (Ma et al., 2021), and CC-CCII segmentation dataset (Zhang et al., 2020). Table 1 provides a summary of these datasets. These datasets will be used to evaluate the segmentation performance of the proposed architecture on binary and multi-class segmentation tasks. In the binary segmentation, the labels are divided into two classes: background and infection region. In the multi-class segmentation, the labels are divided into three classes: background, GGO, and CON.

The COVID-19 CT segmentation (Radiologists, 2019) dataset consists of 100 axial CT images (slices) from over 40 COVID-19 infected patients. It includes multi-class segmentation labels and will be used for the multi-class segmentation task.

Segmentation dataset nr.2 (Radiologists, 2019) contains 9 3D CT scans with a total of 829 slices. Among these slices, 373 have been annotated by radiologists with binary and multi-class segmentation labels for COVID-19 infection. This dataset will be used for both binary and multi-class segmentation tasks.

The COVID-19-CT-Seg dataset (Ma et al., 2021) comprises 20 COVID-19 CT scans, where all cases are confirmed COVID-19 infections. This dataset has been annotated by experienced radiologists and labeled for binary classification. Among the total of 3520 slices, 1844 slices are infected. It will be used for binary segmentation tasks.

The CC-CCII segmentation dataset (Zhang et al., 2020) consists of 750 CT slices from 150 COVID-19 patients, manually annotated for background, lung field, GGO, and CON segmentation. It will be utilized for both binary and multi-class segmentation tasks.

4.2. Evaluation metrics

The model is evaluated by using the following metrics:

1. **F1 score (F1-S):** The F1-S is the harmonic mean of precision and recall, indicating the balance between the true positive rate and the false positive rate,

$$F1score = 100 \cdot \frac{2 \cdot TP}{2 \cdot TP + FP + FN}. \quad (8)$$

2. **Intersection over union (IoU):** The IoU, also referred to as the Jaccard index, computes the ratio of the intersection to the union of predicted and ground truth regions,

$$IoU = 100 \cdot \frac{TP}{(TP + FP + FN)}. \quad (9)$$

3. **Recall(Rec):** The Rec, also referred to as sensitivity or the true positive rate, quantitatively measures the proportion of true positive predictions among all actual positive instances,

$$Rec = 100 \cdot \frac{TP}{TP + FN}. \quad (10)$$

4. **Specificity (Spec):** The Spec measures the proportion of true negative predictions among all actual negative instances,

$$Spec = 100 \cdot \frac{TN}{FP + TN}. \quad (11)$$

5. **Precision (Prec):** The Prec represents the proportion of true positive predictions among all positive predictions made by the model,

$$Prec = 100 \cdot \frac{TP}{TP + FP}, \quad (12)$$

where TP , TN , FP , FN are True Positives, True Negatives, False Positives, False Negatives, respectively.

4.3. Experimental setup

We conduct model training using the PyTorch framework. The experimental platform consists of an Intel Core i5 13600kf CPU, a single NVIDIA GeForce RTX 3090ti 24GB GPU, and the Windows 11 operating system. We utilize the Adam optimizer and set the batch size to 6, performing 120 epochs of training on the network. The initial learning rate is set to $1e-4$ and is decayed by a factor of 0.1 after the 50th epoch and then again after the 90th epoch. Additionally, we apply data augmentation to the dataset, including random angle rotations ranging from -35 degrees to 35 degrees, as well as random horizontal and vertical flips. In terms of the hybrid loss function, the weights are set as 0.7, 0.3, and 1, respectively.

4.4. Experimental results

For the binary segmentation task, we compared our model with Unet, UNet++, Att-Unet, InfNet, SCOAT-Net, nCoVSeg-Net, and PDEAtt-Unet. Tables 2, 3, and 4 present the experimental results of the proposed model on datasets 2, 3, and 4, respectively. It can be observed that the proposed model achieved superior performance in most metrics across these datasets.

On dataset 2, our model outperformed the best-performing segmentation model, PDEAtt-Unet, with improvements of 4.23 in F1 score, 5.85 in IoU, and 4.90 in Recall. These significant improvements can be attributed to the parallel integration of the capsule network pathway and the U-Net encoder pathway in our model design. Capsule networks excel at capturing and preserving hierarchical relationships between objects, while U-Net is adept at extracting local features from images. Through the pathway coupling mechanism, our model effectively combines the advantages of both networks, resulting in more accurate segmentation of complex COVID-19 lung lesions.

On dataset 3, our model achieved improvements of 1.02 in F1 score, 1.33 in IoU, and 2.40 in Recall compared to PDEAtt-Unet. These enhancements further demonstrate the effectiveness of our model design, particularly in handling the diversity and complexity of different datasets. By integrating the capsule network and U-Net encoder in parallel, our model can more effectively identify and segment various lung lesions caused by COVID-19.

On dataset 4, our model also showed improvements in F1 score, IoU, and Recall compared to PDEAtt-Unet, with increases of 0.1, 0.15, and 1.94, respectively. Although these improvements are relatively smaller, they still indicate the consistency and stability of our model across different datasets. This consistency is due to the pathway coupling mechanism in our model, which allows efficient information flow between the two

Name	Dataset	CT-Scans	Slices
Dataset 1	COVID-19 CT segmentation (Radiologists, 2019)	40	100
Dataset 2	Segmentation dataset nr. 2 (Radiologists, 2019)	9	829
Dataset 3	COVID-19-CT-Seg dataset (Ma et al., 2021)	20	3520
Dataset 4	CC-CCII segmentation dataset (Zhang et al., 2020)	150	450

Table 1. The used datasets.

Model	F1-S	IoU	Rec	Spec	Prec
InfNet	40.86	25.68	35.11	99.06	48.88
SCOATNet	69.39	53.13	56.67	99.83	89.46
nCoVSegNet	55.41	38.32	41.10	99.81	85.01
Unet	66.38	49.68	52.15	99.87	91.30
UNet++	59.29	42.13	43.23	99.93	94.32
Att-Unet	59.32	42.17	45.62	99.79	84.79
PDEAtt-Unet	77.60	63.40	80.69	99.30	74.74
Ours	81.61	68.93	82.79	99.55	80.46

Table 2. Comparative experimental results of binary segmentation task on dataset 2.

Model	F1-S	IoU	Rec	Spec	Prec
InfNet	72.91	57.37	66.48	99.78	80.72
SCOATNet	71.02	55.06	61.35	99.84	84.29
nCoVSegNet	62.48	45.44	50.16	99.86	82.85
Unet	65.82	49.05	53.32	99.88	85.97
UNet++	69.89	53.72	60.69	99.82	82.39
Att-Unet	68.67	52.29	58.34	99.84	83.45
PDEAtt-Unet	75.52	60.67	81.94	99.52	70.03
Ours	78.13	64.11	86.01	99.6	71.56

Table 3. Comparative experimental results of binary segmentation task on dataset 3.

network pathways, enhancing segmentation accuracy and robustness.

In the multi-class segmentation task, we merge dataset 1 and dataset 2 into one multi-class segmentation dataset. On this combined dataset, we compare the proposed model with Unet, Att-Unet, Unet++, CopleNet, AnamNet, SCOAT-Net, and D-TrAttUnet among other models. Table 5 presents the experimental results of the proposed model for multi-class segmentation. It can be observed that the model achieved the best segmentation performance, outperforming the previous state-of-the-art segmentation model D-TrAttUnet by 2.79 in F1 score

Model	F1-S	IoU	Rec	Spec	Prec
InfNet	72.19	56.49	63.62	99.86	83.44
SCOATNet	77.57	63.25	70.66	99.86	85.12
nCoVSegNet	78.06	64.02	74.69	99.82	81.74
Unet	75.49	60.63	69.34	99.84	82.84
UNet++	77.45	63.20	71.55	99.85	84.42
Att-Unet	77.27	62.96	70.48	99.87	85.51
PDEAtt-Unet	79.38	65.81	82.52	99.72	76.47
Ours	80.90	67.93	87.19	99.66	75.46

Table 4. Comparative experimental results of binary segmentation task on dataset 4.

and 3.25 in IoU for the GGO classification. For the CON classification, the model surpasses the previous best segmentation model D-TrAttUnet by 2.00 in F1 score and 1.94 in IoU. Additionally, unlike D-TrAttUnet, the model does not use multiple layers of transformers, resulting in significantly reducing the number of model parameters by almost an order of magnitude compared to D-TrAttUnet.

4.5. Ablation study

To further validate the efficacy of CAD-Unet and its individual components, ablation experiments are conducted on four datasets for two tasks. Binary segmentation results on dataset 2, dataset 3, and dataset 4 are summarized in Table 6, while multi-class segmentation results on dataset 1 and dataset 2 are presented in Table 7. These experiments evaluate the effects of the capsule layer, dual decoders, and attention gate.

In the binary segmentation task, we initially examine the enhancement of the CAD-Unet module on the baseline model (Unet). As shown in No.1 and No.2 of Table 6, incorporating the capsule module leads to improvements in F1 score by 2.80, 1.40, and 0.65 on the three datasets, with varying degrees of enhancement in other metrics. Subsequently, the impact of the capsule, dual decoders, and attention gate modules on the binary segmentation capability of the proposed CAD-Unet is investigated, from No.3 to No.6 as depicted in Table 6. Disabling the capsule results in a decrease in F1 score by 11.44, 1.51, and 1.01 on the three datasets, which indicates the critical role of the capsule layer in capturing hierarchical spatial relationships and enhancing feature representation, significantly contributing to the accuracy of the model. Following the deactivation of the attention gate, F1 scores decrease by 6.74, 0.39, and 0.24 on the three datasets, while deactivating the dual decoders lead to even larger decreases of 15.51, 2.51, and 0.34. These findings suggest that the attention gate and dual decoders in CAD-Unet also bring significant improvements to segmentation performance in binary segmentation tasks. The introduction of dual decoders helps the network focus on the lung region, while the attention gate design enables the model to concentrate more on crucial spatial information, thereby enhancing the recognition of subtle features.

In the multi-class segmentation task, similar ablation experiments are conducted. As shown in Table 7, akin to the results in the binary segmentation task, the CAD-Unet module demonstrates a noticeable performance improvement over the baseline model (Unet). Incorporating the capsule into the baseline model results in F1 score improvements of 2.09 and 23.93 percentage points for GOO and CON classifications, respectively. Disabling the capsule in CAD-Unet leads to decreases of 3.2 and 3.09 in F1 score for GOO and CON classifications. This

Model	GGO		Consolidation		Params
	F1-S	IoU	F1-S	IoU	
Unet	65.81	49.06	31.35	19.26	~
Att-Unet	64.81	47.97	39.04	24.48	~
Unet++	65.69	48.92	31.31	18.75	~
CopleNet	60.44	43.33	29.70	17.90	~
AnamNet	65.10	48.36	31.97	19.18	~
SCOATNET	65.77	49.09	43.52	27.83	~
D-TrAttUnet	67.25	50.67	55.24	38.16	105.81M
Ours	70.71	54.69	59.61	42.47	15.05M

Table 5. Comparative experimental results of multi-label segmentation task on dataset 1 and dataset 2.

indicates that the capsule module plays a crucial role in capturing hierarchical relationships between different categories, enhancing the model’s ability to handle multi-class segmentation tasks. Following this, the effects of the attention gate and dual decoders on multi-class segmentation capability are validated. Disabling the attention gate in CAD-Unet results in F1 score decreases of 2.62 and 3.24 for GOO and CON classifications, while disabling the dual decoders leads to F1 score decreases of 0.87 and 3.72 for GOO and CON classifications. This suggests that the attention gate and dual decoders modules also play positive roles in enhancing model performance in multi-class segmentation tasks.

In summary, through in-depth analysis of ablation experiments, we conclude that the capsule module, dual decoders, and attention gate in CAD-Unet are indispensable components, collectively contributing to the outstanding performance of the model in medical image segmentation tasks. These experiments confirm the effectiveness of our proposed architecture and provide valuable insights for future research in deep learning for medical image segmentation. In future, we will continue to optimize these components, expand their applicability, and explore other potential methods to enhance model performance.

5. Discussion

To visually demonstrate the efficacy of our proposed model in addressing both binary and multi-class segmentation tasks for COVID-19 lung CT lesion identification, we conducted a qualitative examination of the segmentation outcomes for both scenarios. Figure 5 provides a visual representation of partially predicted masks alongside the ground truth (GT) for the binary segmentation task, derived from three distinct datasets. The proposed model is compared with Unet++, nCoVSeg, SCOAT-Net, and PDAAtt-Unet models. The results clearly demonstrate the superior performance of the predicted masks by our model, surpassing the other four models in terms of accurately encompassing the entire lesion region and exhibiting more precise and well-defined segmentation boundaries.

This underscores the capability of the model in effectively addressing binary segmentation challenges associated with COVID-19 lung lesions. The predicted masks produced by our model consistently demonstrate a propensity to encapsulate intricate lesion shapes while displaying sharper and more precise

boundaries compared to the alternative models.

Figure 6 illustrates the visualization of partially predicted masks and GT for the multi-class segmentation task from two datasets, using our proposed model along with Unet++, SCOAT-Net, Anamnet, and D-TrAttUnet models. Comparing the predicted masks and GT of other models, the first row of images shows that the proposed model captures more complete CON class masks. The second row demonstrates the superior segmentation performance of our model on small target regions. The third row indicates that our model obtains more accurate target shape information, while the fourth row shows that we achieve more complete target segmentation masks in the GOO class.

In conclusion, our comprehensive qualitative analysis provides evidence suggesting that the proposed model performs favorably compared to current alternatives in addressing binary and multi-class segmentation challenges inherent to COVID-19 lung CT lesion identification. The visual evidence presented here indicates that the model effectively captures intricate lesion morphology and delineates their boundaries with accuracy. Collectively, these advancements may enhance medical image analysis, potentially supporting medical practitioners in their efforts to manage the evolving landscape of the COVID-19 pandemic.

6. Conclusions

The outbreak of COVID-19 has presented significant challenges to global health. Lung CT imaging plays a crucial role in the early diagnosis and treatment of COVID-19 patients. This paper aims to develop an efficient and accurate lung CT lesion segmentation method to assist clinicians in quickly obtaining lesion information for more precise diagnosis and treatment. Our proposed CAD-Unet architecture combines the Unet encoder pathway and capsule encoder pathway in parallel to extract richer local, global, and long-range dependent features. Furthermore, to address the limitations of the BCE loss function in segmenting infection edges, we have incorporated an edge loss component.

To assess the effectiveness of the proposed method, we conducted evaluations on two tasks: binary segmentation and multi-class segmentation. In addition, we compared our method with three baselines and five state-of-the-art architectures for

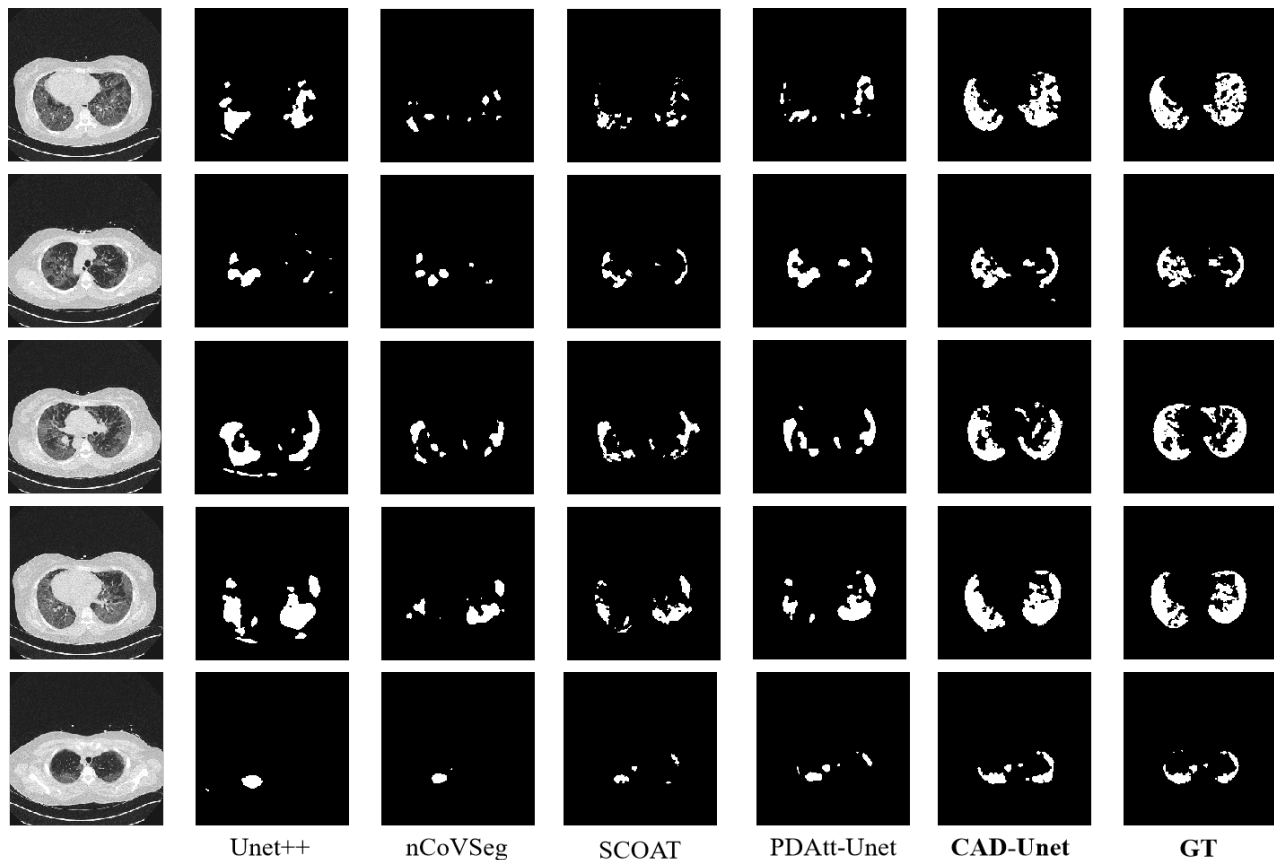


Fig. 5. Visual comparison of a binary segmentation model trained with different segmentation architectures for binary COVID-19 segmentation using dataset 2, dataset 3 and dataset 4.

COVID-19 segmentation. The experimental results demonstrate that our method outperforms all the mentioned architectures in common evaluation metrics for both binary and multi-class segmentation tasks. Furthermore, we performed ablation experiments to validate the effectiveness of the components in our proposed model. In future work, we will explore the potential of combining capsule networks with traditional segmentation models and applying them to a wider range of medical image segmentation tasks.

References

- Ai, T., Yang, Z., Hou, H., Zhan, C., Chen, C., Lv, W., Tao, Q., Sun, Z., Xia, L., 2020. Correlation of chest ct and rt-pcr testing for coronavirus disease 2019 (covid-19) in china: a report of 1014 cases. *Radiology* 296, E32–E40.
- Bougourzi, F., Distant, C., Dornaika, F., Taleb-Ahmed, A., 2023a. D-trattunet: Dual-decoder transformer-based attention unet architecture for binary and multi-classes covid-19 infection segmentation. *arXiv preprint arXiv:2303.15576*.
- Bougourzi, F., Distant, C., Dornaika, F., Taleb-Ahmed, A., 2023b. Pdatt-unet: Pyramid dual-decoder attention unet for covid-19 infection segmentation from ct-scans. *Medical Image Analysis* 86, 102797.
- Chen, J., Wu, L., Zhang, J., Zhang, L., Gong, D., Zhao, Y., Chen, Q., Huang, S., Yang, M., Yang, X., et al., 2020. Deep learning-based model for detecting 2019 novel coronavirus pneumonia on high-resolution computed tomography. *Scientific reports* 10, 19196.
- Choi, J., Seo, H., Im, S., Kang, M., 2019. Attention routing between capsules, in: *Proceedings of the IEEE/CVF international conference on computer vision workshops*, pp. 0–0.
- Fan, D.P., Zhou, T., Ji, G.P., Zhou, Y., Chen, G., Fu, H., Shen, J., Shao, L., 2020. Inf-net: Automatic covid-19 lung infection segmentation from ct images. *IEEE transactions on medical imaging* 39, 2626–2637.
- Kucirka, L.M., Lauer, S.A., Laeyendecker, O., Boon, D., Lessler, J., 2020. Variation in false-negative rate of reverse transcriptase polymerase chain reaction-based sars-cov-2 tests by time since exposure. *Annals of internal medicine* 173, 262–267.
- LaLonde, R., Xu, Z., Irmakci, I., Jain, S., Bagci, U., 2021. Capsules for biomedical image segmentation. *Medical image analysis* 68, 101889.
- Lei, J., Li, J., Li, X., Qi, X., 2020. Ct imaging of the 2019 novel coronavirus (2019-ncov) pneumonia. *Radiology* 295, 18–18.
- Lian, S., Luo, Z., Zhong, Z., Lin, X., Su, S., Li, S., 2018. Attention guided u-net for accurate iris segmentation. *Journal of Visual Communication and Image Representation* 56, 296–304.
- Liu, J., Dong, B., Wang, S., Cui, H., Fan, D.P., Ma, J., Chen, G., 2021. Covid-19 lung infection segmentation with a novel two-stage cross-domain transfer learning framework. *Medical image analysis* 74, 102205.
- Ma, J., Wang, Y., An, X., Ge, C., Yu, Z., Chen, J., Zhu, Q., Dong, G., He, J., He, Z., et al., 2021. Toward data-efficient learning: A benchmark for covid-19 ct lung and infection segmentation. *Medical physics* 48, 1197–1210.
- Ng, M.Y., Lee, E.Y., Yang, J., Yang, F., Li, X., Wang, H., Lui, M.M.s., Lo, C.S.Y., Leung, B., Khong, P.L., et al., 2020. Imaging profile of the covid-19 infection: radiologic findings and literature review. *Radiology: Cardiothoracic Imaging* 2, e200034.
- Oktay, O., Schlemper, J., Folgoc, L.L., Lee, M., Heinrich, M., Misawa, K., Mori, K., McDonagh, S., Hammerla, N.Y., Kainz, B., et al., 2018. Attention u-net: Learning where to look for the pancreas. *arXiv preprint arXiv:1804.03999*.
- Paluru, N., Dayal, A., Jenssen, H.B., Sakinis, T., Cenkeramaddi, L.R., Prakash, J., Yalavarthy, P.K., 2021. Anam-net: Anamorphic depth embedding-based lightweight cnn for segmentation of anomalies in covid-19 chest ct images. *IEEE Transactions on Neural Networks and Learning Systems* 32, 932–946.
- Pan, F., Ye, T., Sun, P., Gui, S., Liang, B., Li, L., Zheng, D., Wang, J., Hesketh,

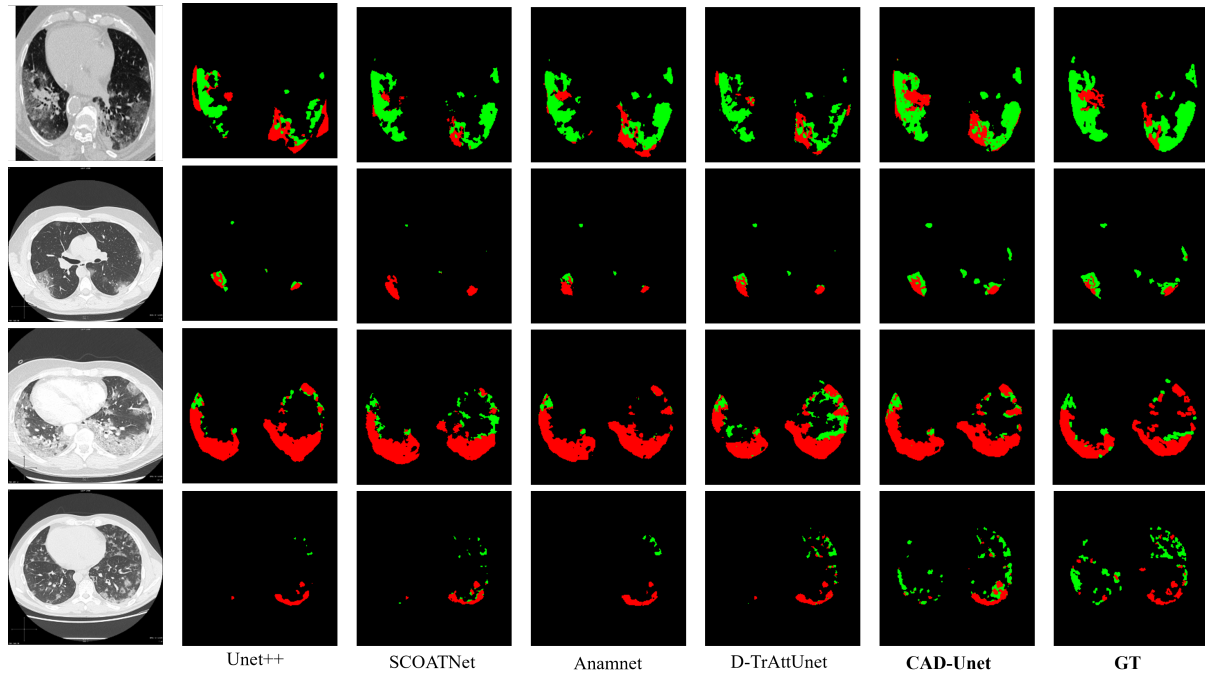


Fig. 6. Visual comparison of a segmentation model trained with different segmentation architectures for multi-classes (No-infection, GGO and CON) COVID-19 infection segmentation using dataset 1 and dataset 2. GGO is presented by the green color and CON by the red color.

No.	Architecture	Ablation			Dataset 2			Dataset 3			dataset 4		
		Cap	AG	DD	F1-S	IoU	Rec	F1-S	IoU	Rec	F1-S	IoU	Rec
1	Unet(baseline)	×	×	×	67.37	50.8	58.09	74.70	59.62	75.81	79.22	66.56	84.22
2	Cap	✓	×	×	70.17	54.05	59.46	76.10	61.42	81.60	79.89	66.52	86.52
3	AG&DD	×	✓	✓	69.97	53.81	57.44	76.62	62.11	81.15	79.81	66.40	85.51
4	Cap&DD	✓	×	✓	74.87	59.84	65.53	77.74	63.59	80.48	80.66	67.59	86.12
5	Cap&AG	✓	✓	×	66.10	49.36	52.23	75.62	60.80	80.11	80.56	67.45	85.07
6	Cap&AG&DD	✓	✓	✓	81.61	68.93	82.79	78.13	64.11	86.01	80.90	67.93	87.19

Table 6. The results of ablation experiments for binary segmentation tasks. The impact of three modules, namely Cap, AG, and DD, on the overall architectural performance in binary segmentation is validated on dataset 2, dataset 3, and dataset 4.

R.L., Yang, L., et al., 2020. Time course of lung changes on chest ct during recovery from 2019 novel coronavirus (covid-19) pneumonia. *Radiology*. Radiologists, 2019. Covid-19 ct-scans segmentation datasets. Available at: <http://medicalsegmentation.com/covid19/>. Last visited: 18-08-2021.

Ronneberger, O., Fischer, P., Brox, T., 2015. U-net: Convolutional networks for biomedical image segmentation, in: *Medical Image Computing and Computer-Assisted Intervention—MICCAI 2015: 18th International Conference, Munich, Germany, October 5-9, 2015, Proceedings, Part III 18*, Springer. pp. 234–241.

Sabour, S., Frosst, N., Hinton, G.E., 2017. Dynamic routing between capsules. *Advances in neural information processing systems* 30.

Survarachakan, S., Johansen, J.S., Pedersen, M.A., Amani, M., Lindseth, F., 2020. Capsule nets for complex medical image segmentation tasks., in: *CVCS*.

Tran, M., Vo-Ho, V.K., Le, N.T., 2022. 3dconvcaps: 3dunet with convolutional capsule encoder for medical image segmentation, in: *2022 26th International Conference on Pattern Recognition (ICPR)*, IEEE. pp. 4392–4398.

Vantaggiato, E., Paladini, E., Bougourzi, F., Distante, C., Hadid, A., Taleb-Ahmed, A., 2021. Covid-19 recognition using ensemble-cnns in two new chest x-ray databases. *Sensors* 21, 1742.

Wang, G., Liu, X., Li, C., Xu, Z., Ruan, J., Zhu, H., Meng, T., Li, K., Huang, N., Zhang, S., 2020a. A noise-robust framework for automatic segmentation of covid-19 pneumonia lesions from ct images. *IEEE Transactions on Medical Imaging* 39, 2653–2663.

Wang, W., Xu, Y., Gao, R., Lu, R., Han, K., Wu, G., Tan, W., 2020b. Detection

of sars-cov-2 in different types of clinical specimens. *Jama* 323, 1843–1844.

Wu, Z., Su, L., Huang, Q., 2019. Stacked cross refinement network for edge-aware salient object detection, in: *Proceedings of the IEEE/CVF international conference on computer vision*, pp. 7264–7273.

Zhang, K., Liu, X., Shen, J., Li, Z., Sang, Y., Wu, X., Zha, Y., Liang, W., Wang, C., Wang, K., et al., 2020. Clinically applicable ai system for accurate diagnosis, quantitative measurements, and prognosis of covid-19 pneumonia using computed tomography. *Cell* 181, 1423–1433.

Zhang, Z., Fu, H., Dai, H., Shen, J., Pang, Y., Shao, L., 2019. Et-net: A generic edge-attention guidance network for medical image segmentation, in: *Medical Image Computing and Computer Assisted Intervention—MICCAI 2019: 22nd International Conference, Shenzhen, China, October 13–17, 2019, Proceedings, Part I 22*, Springer. pp. 442–450.

Zhao, J.X., Liu, J.J., Fan, D.P., Cao, Y., Yang, J., Cheng, M.M., 2019. Egnets: Edge guidance network for salient object detection, in: *Proceedings of the IEEE/CVF international conference on computer vision*, pp. 8779–8788.

Zhao, S., Li, Z., Chen, Y., Zhao, W., Xie, X., Liu, J., Zhao, D., Li, Y., 2021. Scoat-net: A novel network for segmenting covid-19 lung opacification from ct images. *Pattern Recognition* 119, 108109.

Zhou, Z., Rahman Siddiquee, M.M., Tajbakhsh, N., Liang, J., 2018. Unet++: A nested u-net architecture for medical image segmentation, in: *Deep Learning in Medical Image Analysis and Multimodal Learning for Clinical Decision Support: 4th International Workshop, DLMIA 2018, and 8th International Workshop, ML-CDS 2018, Held in Conjunction with MICCAI 2018, Granada, Spain, September 20, 2018, Proceedings 4*, Springer. pp. 3–11.

No.	Architecture	Ablation			GGO			CON		
		Cap	AG	DD	F1-S	IoU	Rec	F1-S	IoU	Rec
1	Unet(baseline)	×	×	×	65.81	50.13	49.06	31.35	15.45	19.26
2	Cap	✓	×	×	67.90	51.45	59.40	55.28	38.22	61.31
3	AG&DD	×	✓	✓	67.51	51.09	58.99	56.52	39.41	59.47
4	Cap&DD	✓	×	✓	68.09	51.67	58.97	56.37	39.25	62.86
5	Cap&AG	✓	✓	×	69.84	53.67	63.53	55.89	38.80	58.47
6	Cap&AG&DD	✓	✓	✓	70.71	54.69	63.34	59.61	42.47	64.59

Table 7. The results of ablation experiments for multi-segmentation tasks. The influence of three modules, namely Cap, AG, and DD, on the overall architectural performance in multi-valued segmentation is verified on the combined dataset of dataset 1 and dataset 2.